applied sciences

MDPI

Article

Doppler Wind Lidar Observations of Wind Shear Associated with Low-Level Jets in a Valley Terrain

Huiyu Ding [1], Dandan Zhao [1,2,*], Lian Duan [1], Xiaole Pan [2] and Tianyi Wang [3]

[1] College of Aviation Meteorology, Civil Aviation Flight University of China, Guanghan 618307, China; dinghy@cafuc.edu.cn (H.D.); cafcdl@163.com (L.D.)
[2] State Key Laboratory of Atmospheric Boundary Layer Physics and Atmospheric Chemistry (LAPC), Institute of Atmospheric Physics, Chinese Academy of Sciences, Beijing 100029, China; panxiaole@mail.iap.ac.cn
[3] Meteorological Service Center of Hubei Province, Wuhan 430074, China; tianyiwang@smail.nju.edu.cn
* Correspondence: zhaodandan@cafuc.edu.cn

Abstract

Low-level wind shear (LLWS) poses a critical threat to aviation safety, especially at high-altitude airports located in valley environments. However, the formation mechanisms of LLWS with low-level jets (LLJs) remain poorly understood under high-altitude valley conditions. In this study, high-resolution Doppler lidar observations collected during March–April 2024 were used to investigate the characteristics of low-level wind fields, LLJs, and LLWS, as well as their relationship in an airport environment. The results reveal pronounced diurnal variations in the low-level circulation, with easterly winds dominating from early morning to late morning, westerly winds prevailing in the afternoon, and southerly winds occurring at night. LLJ events exhibit a strong diurnal cycle, with the highest frequency occurring during 02:00–10:00 LT, and jet cores are mainly distributed between 200 and 300 m. The observed LLJs are predominantly easterly, with typical maximum wind speeds of 8–10 m s^{-1}. The development of LLJs is related to enhanced LLWS, although the temporal correspondence between LLJ intensity and LLWS evolution varies among individual events. The vertical shear structure is closely related to LLJ characteristics, including jet core height and wind speed distribution. Case analyses further demonstrate that the spatial evolution of LLWS follows the directional migration of LLJs, with the high wind-speed region shifting from easterly sectors in the morning to westerly sectors in the afternoon and southerly sectors at night. These findings provide new observational insights into LLJ-related LLWS processes under high-altitude valley environments and contribute to improved understanding of low-level wind hazards in complex airport environments.

Keywords: low-level wind shear; low-level jets; lidar; valley; remote sensing detection

Academic Editor: Harry D. Kambezidis

Received: 07 September 2026
Revised: 08 October 2026
Accepted: 29 October 2026
Published: 30 October 2026

Copyright: © 2026 by the authors. Licensee MDPI, Basel, Switzerland. This article is an open access article distributed under the terms and conditions of the Creative Commons Attribution (CC BY) license.

1. Introduction

Low-level wind shear (LLWS) refers to rapid changes in wind speed and/or direction over short vertical or horizontal distances within the lower atmosphere [1,2]. It is one of the most critical meteorological hazards affecting aviation safety. Strong LLWS near airports can lead to sudden changes in aircraft airspeed and flight trajectory, particularly during takeoff and landing phases when aircraft are highly sensitive to wind variations [1,3]. Therefore, accurate detection and understanding of LLWS characteristics are

essential for improving aviation safety and developing effective wind shear warning systems [4,5].

LLWS can be generated by various atmospheric processes, including frontal passages [2], convection [6], boundary-layer transitions [7], low-level jets (LLJs) [8], and terrain-induced flows [9,10]. Among these mechanisms, LLJs are considered one of the major contributors to strong low-level wind gradients due to their characteristic vertical wind speed maxima and sharp transitions between the jet core and surrounding airflows [11]. LLJs frequently occur within the nocturnal boundary layer under stable stratification conditions, when reduced turbulent mixing allows horizontal momentum to accumulate above the surface layer [7]. The formation and evolution of LLJs can produce significant vertical and directional wind shear, thereby increasing the likelihood of hazardous low-level wind conditions for aviation operations [12].

In recent years, increasing attention has been devoted to understanding the characteristics and mechanisms of LLWS and LLJs through field observations, numerical simulations, and remote sensing techniques [13,14]. Advances in Doppler lidar and radar wind profiler observations have provided high-resolution measurements of low-level wind structures, revealing substantial temporal variability associated with boundary-layer evolution and low-level flow acceleration [15,16]. Meanwhile, LLJ studies have primarily focused on jet formation mechanisms, vertical structures, diurnal variability, and their impacts on turbulence and wind shear [17,18]. However, the relationship between LLJ evolution and LLWS generation remains highly dependent on local atmospheric conditions, including terrain complexity, boundary-layer stability, and background circulation [19]. In particular, observations of LLJ structures and their direct linkage with LLWS under complex terrain environments remain relatively limited.

The Tibetan Plateau (TP), characterized by its high elevation, complex topography, and strong thermal forcing [20,21], provides a unique environment for investigating low-level atmospheric circulation and boundary-layer processes. The valley terrain across the TP can significantly modify local wind fields through terrain channeling effects and thermally driven valley circulations. Airports located in high-altitude regions of the TP are particularly vulnerable to hazardous wind conditions due to terrain-induced flows, pronounced diurnal thermal variations, and complex boundary-layer structures [22–24]. Lhasa Gonggar Airport (ZULS), situated in the middle reaches of the Yarlung Zangbo River valley at an elevation of approximately 3600 m, is surrounded by mountains with large elevation differences, with high mountains located on both sides of the valley. The narrow valley terrain and the surrounding steep mountains strongly constrain low-level airflow, resulting in highly complex wind structures near the airport [25]. Previous studies in the Tibetan Plateau region have mainly focused on wind climatology [26,27], turbulence characteristics [28], mountain-valley circulation [29], and aviation-related meteorological hazards [30]. However, detailed observational investigations of LLJ structures and their relationship with LLWS under terrain conditions at Lhasa Airport remain scarce.

Despite previous advances, several uncertainties remain regarding LLJ-related LLWS processes in high-altitude valley airport environments. First, most existing studies have focused on the statistical characteristics of either LLWS or LLJs separately, while the coupling relationship between LLJ evolution and LLWS development has not been fully quantified [30,31]. Second, traditional radiosonde observations have limited temporal and spatial coverage, making them difficult to resolve rapid changes in low-level wind structures [32]. Third, the influence of LLJ directional transitions on the spatial distribution of LLWS has received relatively little attention, especially in high-altitude valley regions where terrain-induced flow variations can significantly affect low-level wind structures and wind shear characteristics. Unlike our previous study [33], which focused on optimizing an LLWS detection algorithm, the present study focuses on the

physical relationship between LLJ evolution and LLWS development. This study utilizes high-resolution Doppler wind lidar observations at Lhasa Gonggar Airport to investigate the characteristics of low-level wind fields, LLWS occurrence, and LLJ structures, and further explores the relationship between LLJ evolution and LLWS development in a valley-based high-altitude airport environment. The results provide new observational evidence for understanding low-level wind hazards in valley regions of the Tibetan Plateau and contribute to improved aviation meteorological monitoring and forecasting. The remainder of this study is organized as follows: Section 2 describes the study area, field experiment, and retrieval methods. Section 3 presents the results. Section 4 provides the discussion and conclusions, respectively.

2. Data and Methods

2.1. Site and Data

The study area is located around Lhasa Gonggar Airport (ZULS), Tibet Autonomous Region, China. The region is situated in the southern Tibetan Plateau (Figure 1a), within the middle reaches of the Yarlung Zangbo River valley, approximately between 28.5–30.5°N and 89.5–92.5°E. Characterized by high elevation and a deep valley terrain, the area exhibits unique atmospheric and topographic conditions. The airport is located in the narrow Yarlung Zangbo River valley and is surrounded by high mountains, with surrounding peaks reaching elevations of up to 7000 m. The valley terrain and large elevation differences strongly constrain low-level airflow and contribute to complex wind structures near the airport. Therefore, under such valley terrain conditions, low-level wind shear and low-level jets are frequently observed, posing significant challenges to aviation safety and flight operations.

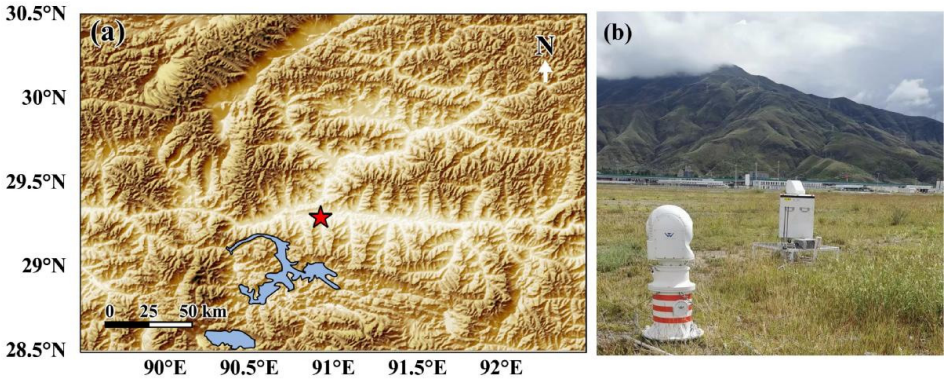


Figure 1. (**a**) Geographical location and topography of the study area (The red star indicates the location of Lhasa Gonggar Airport); (**b**) outdoor view of the Doppler wind lidar (DWL).

A Doppler wind lidar (DWL) was deployed to retrieve wind speed and wind direction by emitting coherent laser pulses and analyzing the Doppler shift of aerosol- and molecule-backscattered signals [34,35]. Strictly, the DWL directly measures the line-of-sight radial velocity, while horizontal wind information is obtained through subsequent retrieval algorithms. Two standard scanning strategies were implemented: plan-position-indicator (PPI) and Doppler-beam-swinging (DBS) modes.

In PPI mode, a fixed elevation angle of 3° was applied to resolve horizontal wind structures associated with aircraft arrival and departure corridors. Azimuthal scanning covered 360° with a 4° step size, yielding a complete scan cycle of approximately 8 min. The radial range resolution was set to 100 m, providing detailed horizontal sampling of the wind field over extended distances. The horizontal wind fields from PPI scans were

retrieved using the Velocity-Azimuth Display (VAD) method proposed by Browning and Wexler [36]. In the VAD approach, the Doppler lidar performs conical scanning at a fixed elevation angle, and the radial velocity varies periodically with azimuth angle due to the projection of the horizontal wind vector onto the laser beam. Under the assumption of horizontal homogeneity within the scanning volume, the radial velocity distribution along a complete azimuthal scan can be described by a harmonic function. The horizontal wind speed and wind direction are obtained from the amplitude and phase of the first-order harmonic component of the radial velocity variation with azimuth angle.

In DBS mode, line-of-sight velocities were acquired at multiple elevation angles to reconstruct vertical wind profiles. The DBS method retrieves wind information from multiple tilted laser beams based on the geometric relationship between the measured radial velocities and the three-dimensional wind vector. Assuming horizontal homogeneity within the sampling volume, radial velocity measurements from different beam directions are combined to derive horizontal wind speed, horizontal wind direction, and vertical velocity. The resulting vertical resolution was 28 m, enabling high-resolution characterization of vertical wind shear and boundary-layer structure. The main observational configurations and scanning parameters of the PPI and DBS modes are summarized in Table 1.

It should be noted that the measurement capability of Doppler wind lidar can be influenced by atmospheric conditions, particularly fog, low clouds, and precipitation. These conditions may reduce aerosol backscatter signals and consequently affect the availability of wind-profile retrievals. During the observation period, concurrent observations of visibility, cloud-base height, and precipitation were not available at the observation site. Therefore, the quantitative impacts of these meteorological conditions on lidar measurement capability could not be evaluated in this study. The Doppler lidar dataset collected during March–April 2024 contained 277,875 DBS wind profiles, providing the observational basis for LLJ identification and subsequent analysis.

Table 1. Parameters and technical specifications of the Doppler Wind Lidar.

Parameter	Technical Specifications
Wavelength	1.55 μm
Elevation angle	3°
Azimuth range	0–360° (Δφ = 4°)
Horizontal range resolution	100.25 m
Vertical range resolution	28 m
Horizontal detection range	200.25 m–5024.25 m
Vertical detection range	42 m–4627 m
Temporal resolution	3 s (DBS); 8 min (PPI)

2.2. Combination Shear Calculation Method

$$C_{Rs} = \frac{\Delta \vec{V}}{\Delta R} = \frac{\sum_{i=1}^{n} \vec{V}_i - \vec{V}_0}{n \sum_{i=1}^{n} r_i - r_0} \quad (1)$$

$$C_{As} = \frac{\Delta \vec{V}}{\frac{\pi r \Delta\theta}{180}} = \frac{\sum_{i=1}^{n} \vec{V}_i - \vec{V}_0}{\frac{m\pi r_0 \sum_{i=1}^{m} \theta_i - \theta_0}{180}} \quad (2)$$

$$\left|\vec{V}_i - \vec{V}_0\right| = \sqrt{(u_i - u_0)^2 + (v_i - v_0)^2} \quad (3)$$

where V_0 denotes the horizontal wind speed at the selected reference location along the radial direction, and V_i represents the corresponding wind speed measured at the *ith* range gate. u_i and u_0 denote the eastward wind components at the corresponding locations, while v_i and v_0 represent the northward wind components. r_0 and r_i are the radial distances from the radar to the reference point and the *ith* sampling gate, respectively. ΔR is the radial spacing interval, and n denotes the number of valid observations included within a 200 m radial window. In the azimuthal dimension, θ_0 and θ_i represent the azimuth angles of the reference point and the *ith* gate, respectively. $\Delta\theta$ indicates the azimuthal interval, while m refers to the number of data points considered within a 20° azimuthal sector.

The horizontal shear value C_s is then obtained by vectorially combining C_{Rs} and C_{As}:

$$C_s = \sqrt{C_{Rs}{}^2 + C_{As}{}^2} \quad (4)$$

This integrated shear parameter provides a quantitative description of the horizontal wind variability derived from lidar PPI observations, thereby offering a more complete assessment of local wind shear characteristics.

2.3. Optimization Method

2.3.1. Optimization Objective

This approach aims to derive a divergence-constrained refined wind-shear field $C_s^*(x,y)$ by incorporating the dynamical influence of horizontal divergence $D(x,y)$ into the original shear field $C_s(x,y)$ [33].

The optimized wind-shear field is expressed as a divergence-modulated correction to the original shear field:

$$C_s^*(x,y) = C_s(x,y) + \lambda D(x,y) \quad (5)$$

where λ represents the relative contribution coefficient of horizontal divergence to the shear field, which is statistically determined through logistic regression analysis.

2.3.2. Mathematical Procedure

(1) The wind field divergence D is calculated as

$$u = -w_s \sin(w_d) \quad (6)$$

$$v = -w_s \cos(w_d) \quad (7)$$

where u and v represent the eastward and northward wind components, respectively; w_s denotes the horizontal wind speed; and w_d represents the meteorological wind direction, defined as the direction from which the wind originates and measured clockwise from true north.

The radial and azimuthal components of the horizontal wind vector were further calculated as:

$$V_r = u\sin\phi + v\cos\phi \tag{8}$$

$$V_\phi = u\cos\phi - v\sin\phi \tag{9}$$

where V_r and V_ϕ denote the radial and azimuthal wind components, respectively, and ϕ represents the azimuth angle of the PPI scan.

The horizontal divergence was then calculated in polar coordinates:

$$D(x,y) = \left| \frac{1}{r}\frac{\partial(rV_r)}{\partial r} + \frac{1}{r}\frac{\partial V_\phi}{\partial \phi} \right| \tag{10}$$

where D represents the magnitude of horizontal divergence and r denotes the radial distance from the lidar.

(2) Divergence-based mask

Based on this threshold criterion, a binary mask function $M(x,y)$ is subsequently established:

$$M(x,y) = \begin{cases} 1, D(x,y) > Q3 \\ 0, D(x,y) \le Q3 \end{cases} \tag{11}$$

In this study, Q3 was calculated from the 75th percentile of the divergence values. The original wind-shear values Cs are retained within the identified mask regions, whereas values outside these regions are removed by assigning zero values, resulting in the divergence-filtered wind-shear field:

$$C_{s,filt} = C_s(x,y) \bullet M(x,y) \tag{12}$$

where $C_s(x,y)$ is the original wind-shear field.

(3) Severe-shear labeling

A binary classification label is defined based on the severe wind-shear threshold (≥0.139 s^{-1}):

$$y(x,y) = \begin{cases} 1, C_s(x,y) > 0.138 \\ 0, C_s(x,y) \le 0.138 \end{cases} \tag{13}$$

(4) Logistic regression

A logistic regression model was applied using $C_{s,filt}$ and D as predictors to quantify the relative contribution of divergence and derive the coefficient λ.

$$p(y=1) = \frac{1}{1+\exp(-(\beta_0 + \beta_1 C_{s,filt} + \beta_2 D))} \tag{14}$$

where β_0 is the intercept, while β_1 and β_2 represent the regression coefficients associated with the original wind shear ($C_{s,filt}$) and wind-field divergence (D), respectively.

The decision boundary of the model is expressed as

$$\beta_0 + \beta_1 C_{s,filt} + \beta_2 D = 0 \tag{15}$$

The contribution of horizontal divergence is quantified through the introduction of the coefficient λ:

$$\lambda = \frac{\beta_2}{\beta_1} \tag{16}$$

(5) Construction of the divergence-constrained refined shear field

Accordingly, the optimized wind-shear field is derived following Equation (5). To maintain physical consistency, negative values are constrained to zero:

$$C_s^*(x,y) = \max\left\{C_s^*(x,y), 0\right\} \tag{17}$$

where $C_s^*(x,y)$ represents the refined wind-shear field after constraining negative values to zero. A positive value of λ indicates a positive statistical contribution of divergence to the refined shear field, whereas a negative value represents an opposite contribution. Since the logistic regression coefficients are derived independently for each PPI scan, β_0, β_1, β_2, and λ vary with different wind-field conditions. The definitions of these parameters are summarized in Table 2.

Table 2. Definitions of parameters used in the optimization method.

Parameter	Definition
Q_3	75th percentile threshold of absolute divergence
β_0	Logistic regression intercept
β_1	Regression coefficient of filtered wind shear
β_2	Regression coefficient of horizontal divergence
λ	Relative contribution coefficient of divergence

2.4. Vertical Wind Shear Calculation

Vertical wind shear is defined as the gradient of the wind vector with respect to altitude. It is calculated as follows:

$$VWSI = \frac{\sqrt{(u_2 - u_1)^2 + (v_2 - v_1)^2}}{z_2 - z_1} \tag{18}$$

where u and v denote the horizontal wind components at the two corresponding heights, z_1 and z_2, respectively.

Furthermore, Gutierrez [37] and Shu [11] reported that LLJs are typically associated with positive wind shear below the jet core and negative wind shear above it. To further investigate the relationship between LLJs and LLWS, this study adopts the wind shear coefficient proposed by Rehman and Al-Abbadi [38]. The calculation is expressed as follows:

$$\alpha = \frac{\ln(v_2) - \ln(v_1)}{\ln(z_2) - \ln(z_1)} \tag{19}$$

When calculating the positive wind shear coefficient below the jet core, v_2 and z_2 represent the jet speed maximum and the jet-core height, respectively. While v_1 and z_1 correspond to the wind speed and height at the surface observation level. For the calculation of the negative wind shear coefficient, v_1 is defined as either the next wind speed minimum above the jet core or the wind speed at 694 m, whichever is lower. z_1 represents the corresponding height of the selected upper-level minimum wind speed.

Based on the wind shear intensity definition recommended by the World Meteorological Organization (WMO), LLWS intensity is classified into four levels, as

listed in Table 3. In this study, LLWS with an intensity reaching the moderate level or above (≥0.068 s^{-1}) is identified as a low-level wind shear (LLWS) event.

Table 3. Low-level wind shear strength standard of World Meteorological Organization.

Level	Wind Shear Strength (s^{-1})
mild	<0.067
moderate	0.068~0.138
severe	0.139~0.206
extreme	>0.206

2.5. Definition of Speed Criteria for LLJ Identification

Based on previous climatological studies of Low-Level Jets over China [39–41], the identification criterion for LLJs in this study is established considering the characteristics of the complex-terrain environment over the Tibetan Plateau. Although classical strong LLJs, such as those observed over the Great Plains of the United States, are often identified using wind speed thresholds of 12–15 m s^{-1}, absolute wind speed thresholds may vary among different regions due to differences in background circulation and underlying surface conditions. Therefore, in this study, LLJs refer to weak low-level jets characterized by distinct low-level wind speed maxima and vertically confined jet structures. The wind speed below 600 m reaches a local maximum U_{max}. Above this level, the wind speed decreases to a local minimum U_{min} at the next higher level. The decrease must be at least 3 m s^{-1}. If this condition is satisfied, the flow is classified as a Low-Level Jet. The jet core height is determined by the height at which U_{max} occurs.

During March–April 2024, DBS observations were collected over 61 valid days at Lhasa Gonggar Airport. Based on the observed wind-profile characteristics and the LLJ identification criteria, 16 LLJ events were identified for further analysis. Considering the different analysis objectives, different temporal resolutions were applied. The 5-min averaged DBS profiles were used to illustrate the detailed temporal evolution of individual LLJ cases, while the 10-min averaged DBS profiles were used for statistical analysis. For the selected 16 LLJ events, 2304 quality-controlled 10-min DBS profiles were retained, among which 638 profiles satisfied the LLJ criteria.

2.6. Turbulent Kinetic Energy (TKE)

Turbulent kinetic energy (TKE) was calculated from DBS-mode lidar observations using the variance method:

$$TKE = \frac{1}{2}(\sigma_u^2 + \sigma_v^2 + \sigma_w^2) \quad (20)$$

where σ_u^2, σ_v^2, and σ_w^2 denote the variances of the zonal, meridional, and vertical wind components, respectively. The three wind components were derived from the retrieved wind speed, wind direction, and vertical velocity. A 10-min averaging interval was used to calculate the velocity variances. The DBS wind profile data were quality-controlled products, and invalid measurements were removed before further analysis.

3. Results and Discussion

The results mainly focus on the wind field structure, the characteristics of LLWS and LLJs, as well as their interrelationships. First, the overall temporal variability of the low-level horizontal wind field and the frequency of LLWS events are investigated. Second, the characteristics of overall LLJs are analyzed, including the temporal, vertical, and directional distributions of their occurrence frequency. Next, the relationship between

low-level wind shear and low-level jets is examined. Finally, two representative LLJ cases are selected for detailed discussion.

3.1. Background Characteristics of Wind Field

Figure 2 presents the wind rose distributions derived from the PPI-mode observations during March–April 2024 at three selected radial distances (1004, 2612, and 4823 m). The corresponding measurement heights (approximately 70, 182, and 336 m) were determined based on the scanning geometry using the relationship between radial distance and elevation angle (height = range × sin(ELE)). The radial axis represents the frequency of wind directions, and different colors indicate different wind speed categories. The figure illustrates the temporal and vertical variations in wind direction and wind speed characteristics during the observation period.

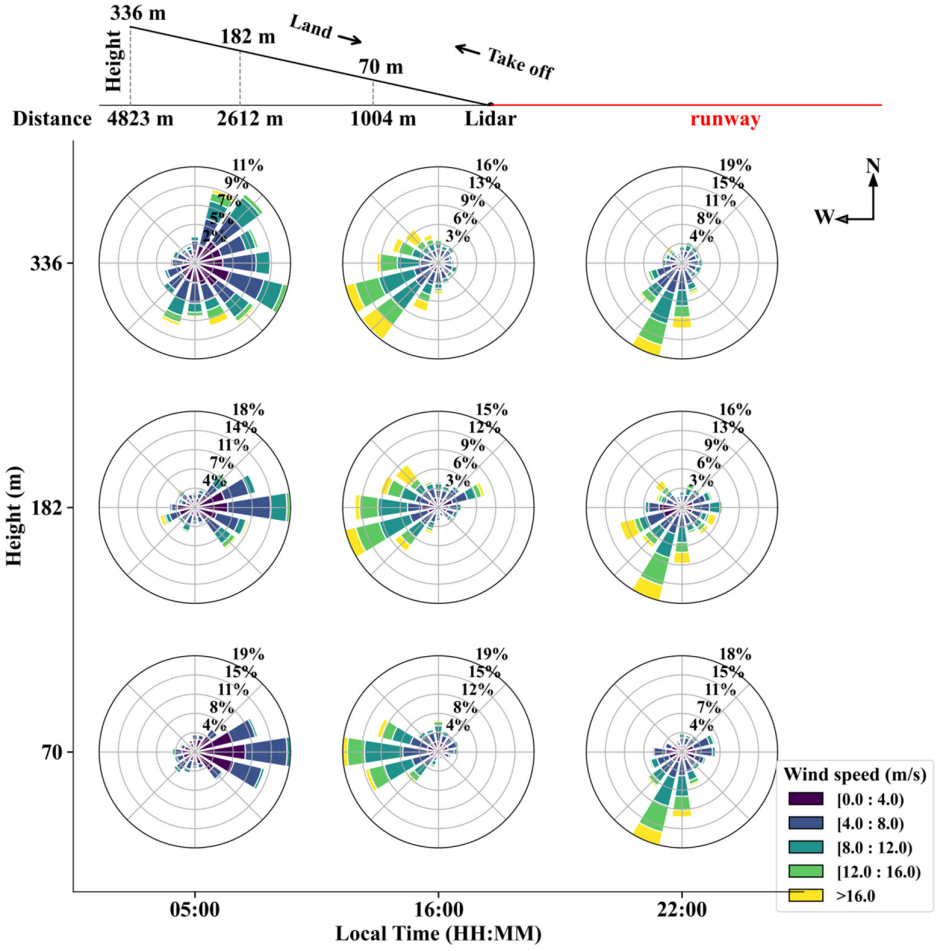


Figure 2. Wind rose distributions at different heights and local times under PPI mode from 1 March to 30 April 2024. The radial axis represents wind direction frequency (%), and different colors indicate wind speed categories. The upper panel illustrates the lidar observation geometry and flight trajectory.

The results show clear diurnal variations in the wind field. At 05:00, easterly winds dominate at different heights, with the maximum occurrence frequency reaching approximately 18–19%. At 16:00, the prevailing wind direction shifts toward the western–southwestern sectors, accompanied by an increased contribution of higher wind speed components, especially at 336 m where the dominant wind frequency reaches about 19%. At 22:00, southerly and southwesterly winds become dominant, with peak frequencies of

approximately 16–19%. Overall, the prevailing wind direction changes significantly throughout the day, indicating evident diurnal evolution of the local wind circulation. Vertically, the wind field also exhibits clear stratification. Higher altitudes show a larger proportion of strong wind components (>12 m·s^{-1}) and a broader wind direction distribution, while the 70 m layer is characterized by relatively weaker and more concentrated winds due to surface friction effects. These results demonstrate that both time-dependent circulation changes and vertical atmospheric structures strongly influence the observed wind characteristics.

Figure 3 presents the azimuthal distributions of the occurrence frequency of LLWS (with intensity ≥ 0.068 s^{-1}), derived from PPI-mode lidar observations at three selected radial distances (1004 m, 2612 m, and 4823 m) during March–April 2024. The radial axis represents the frequency of wind shear occurrence, while the azimuth angle indicates the spatial distribution within the lidar scanning domain. The figure illustrates the temporal and spatial variations in wind shear occurrence along the aircraft approach/departure corridor.

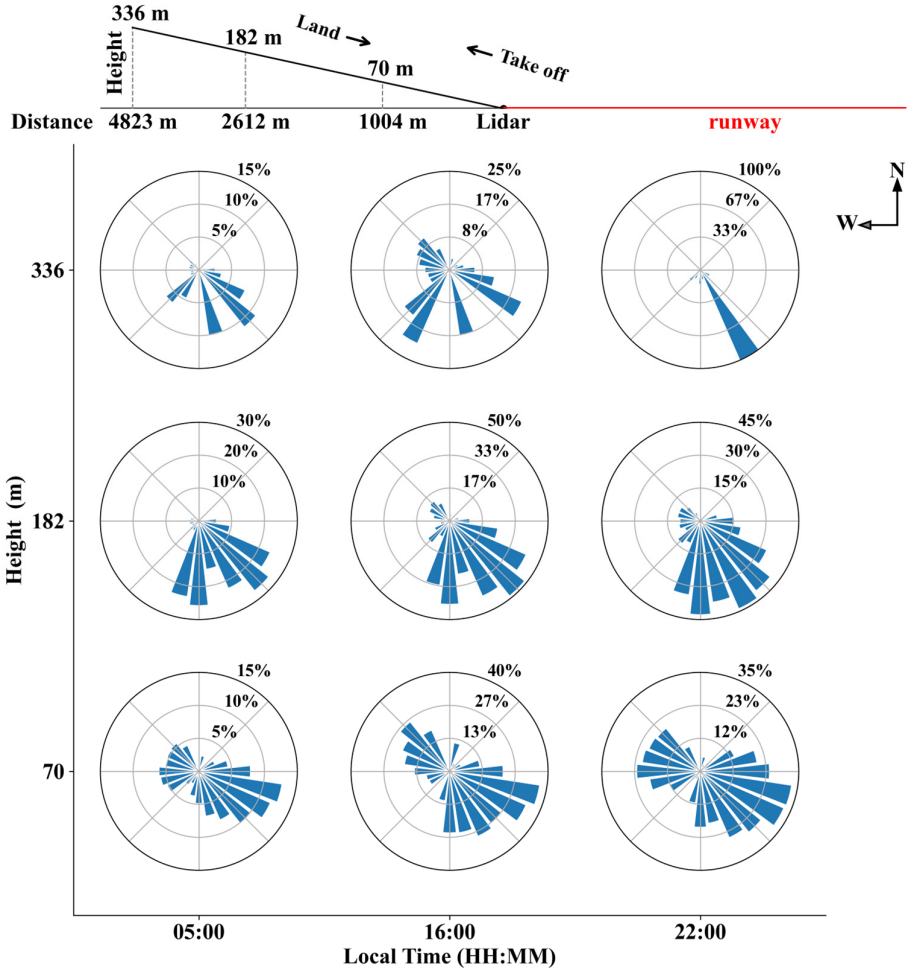


Figure 3. Wind shear frequency distributions at different heights and local times under PPI mode from 1 March to 30 April 2024. The upper panel illustrates the lidar observation geometry and flight trajectory.

The results show clear diurnal and spatial variations in wind shear occurrence frequency. At 05:00, wind shear frequencies are generally low across most azimuth sectors, with relatively limited directional differences. At 16:00, the occurrence frequency

increases, with several sectors reaching 30–50%, particularly at the 1004 m and 2612 m ranges. At 22:00, wind shear occurrence becomes more concentrated in specific azimuth sectors, with the highest frequency observed at 4823 m, approaching 100%. Spatially, wind shear occurrence shows a distinct azimuthal dependence, with higher frequencies primarily observed in the southeast-to-south sectors. Among the three selected radial distances, the 2612 m radial distance exhibits relatively higher wind shear occurrence frequencies, while the distributions at 1004 m and 4823 m show comparatively lower frequencies with different azimuthal patterns. The frequency distribution varies with both radial distance and observation time, indicating heterogeneous wind shear occurrence within the PPI scanning domain.

To investigate the influence of large-scale atmospheric circulation on LLJ occurrence, ERA5 reanalysis data were used to characterize the synoptic background associated with the observed LLJ events. For each event, the 500 hPa geopotential height, temperature, and horizontal wind fields were extracted during a ±2 h period centered on the LLJ peak time (local time). Based on the spatial distribution of the 500 hPa trough/ridge systems and the prevailing flow pattern around Lhasa Gonggar Airport, the 16 LLJ events were manually classified into two synoptic categories: a trough-influenced pattern and a flat westerly flow pattern. The synoptic circulation patterns corresponding to the two LLJ categories are illustrated in Figure 4.

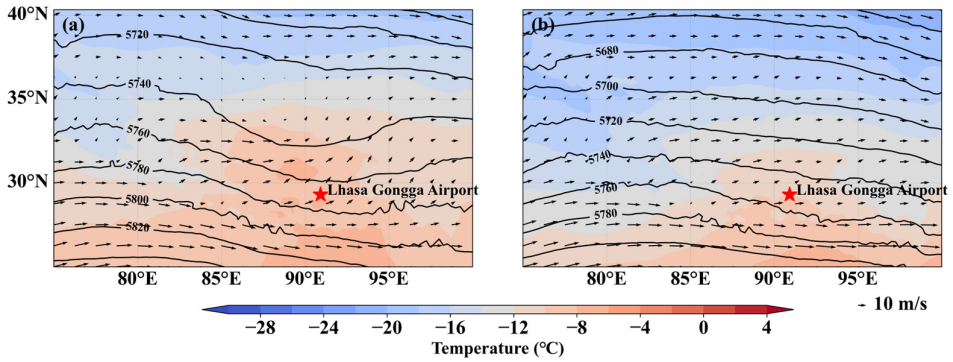


Figure 4. Composite 500 hPa circulation patterns associated with LLJ events over Lhasa Gonggar Airport. (**a**) Trough-influenced pattern (Type 1, N = 6); (**b**) flat westerly flow pattern (Type 2, N = 10). Shaded areas represent air temperature, black contours denote geopotential height (gpm), and vectors indicate horizontal wind fields. The red star marks the location of Lhasa Gonggar Airport.

Six events were identified as the trough-influenced pattern (Type 1), occurring on 25 March, 29 March, 3 April, 6 April, 15 April, and 21 April 2024. The remaining ten events were categorized as the flat westerly flow pattern (Type 2), including events on 2 March, 6 March, 9 March, 12 March, 13 March, 15 March, 30 March, 13 April, 22 April, and 25 April 2024. The classification indicates that LLJ events occurred under different synoptic backgrounds. Type 1 was characterized by the influence of mid-latitude trough systems, with the observation site located near the trough-related circulation region. In contrast, Type 2 occurred under a relatively straight westerly flow background, suggesting that LLJ development can also occur without pronounced trough activity.

3.2. Basic Structure and Statistical Characteristics of LLJ

Based on the LLJ identification criteria applied in this study, wind profiles exhibiting distinct low-level jet characteristics were identified. Figure 5 presents 16 representative LLJ cases selected in this work. These cases cover different dates and local times under various observational conditions. For each case, the most representative time is selected,

and wind speed profiles are shown at 5-min intervals. Overall, the vertical wind profiles exhibit a typical low-level jet structure. Wind speed increases rapidly with height, reaches a local maximum at a certain level, and then decreases or remains nearly constant above it. This structure reflects the strong vertical heterogeneity of momentum within the boundary layer. It is generally associated with the formation of a nocturnal stable boundary layer and the weakening of turbulent mixing near the surface. Intercomparison among cases shows clear variations in jet intensity. The peak wind speed ranges from approximately 5 to 10 m s^{-1}. The jet core height is mainly concentrated between 200 and 300 m. This height range corresponds to the typical top of the stable boundary layer, where vertical wind shear is significantly enhanced.

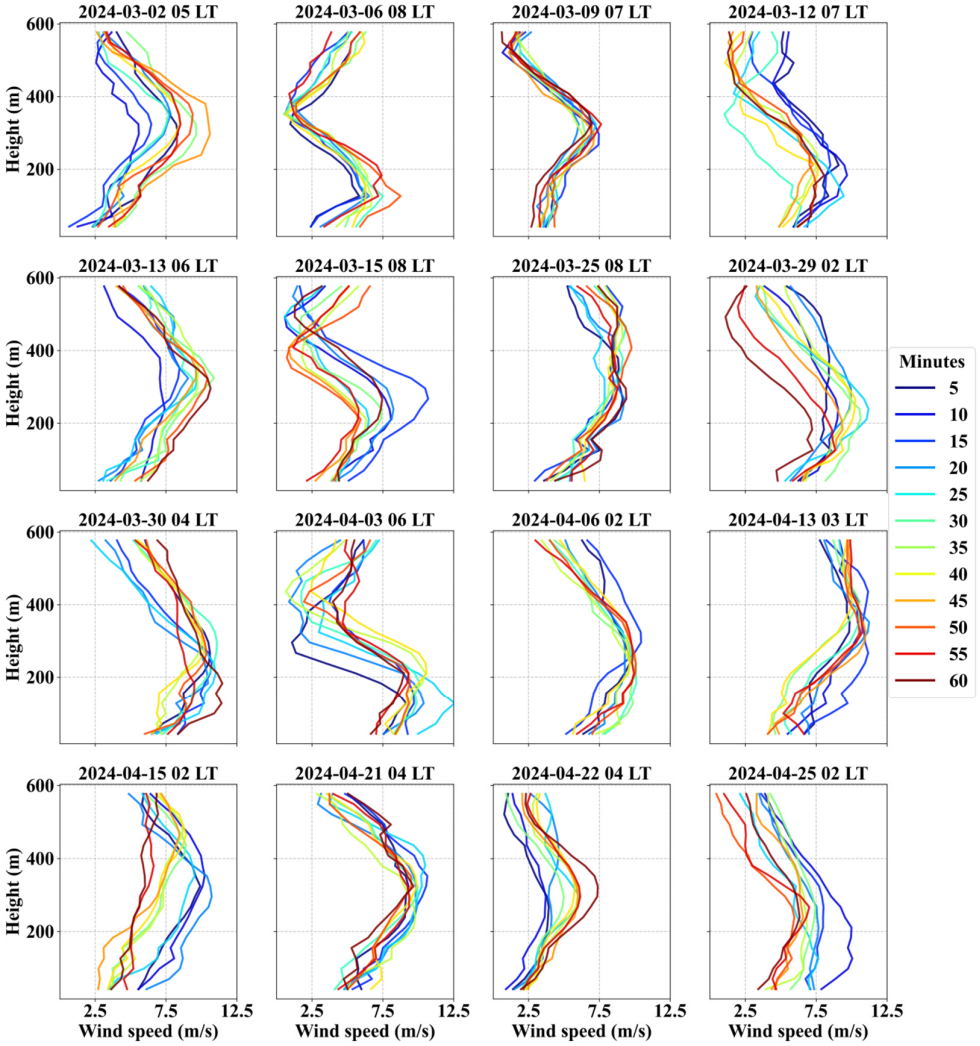


Figure 5. Sample of 5-min wind profiles displaying Low-Level Jets (LLJs). Each panel shows data from a specific night over a one-hour period in local time (LT). The line colors represent the average wind profile values for each 5-min interval within the hour.

Figure 6 presents the temporal, vertical, and directional distributions of LLJ occurrence frequency. The statistics were calculated based on 16 selected LLJ cases, corresponding to 16 observation days with identified LLJ events. These cases contain multiple DBS wind profiles rather than individual instantaneous observations. For the diurnal distribution (Figure 6a), the LLJ occurrence frequency at each local hour was calculated as the ratio of LLJ profiles to all valid DBS profiles at the corresponding hour

during the 16 selected cases. The occurrence frequency is mainly concentrated from early morning to late morning (02:00–10:00 LT). The highest frequency occurs at 04:00 and 05:00 LT, with values exceeding 65%. In contrast, LLJ activity is relatively weak during the afternoon and early evening (13:00–18:00 LT), with frequencies below 10%. This diurnal pattern is closely related to nocturnal boundary-layer stabilization and the weakening of turbulent mixing, which favor momentum accumulation and the formation of LLJ structures. For the vertical distribution (Figure 6b), the occurrence frequency was calculated based on the distribution of LLJ core heights among the identified LLJ profiles. The LLJ cores are mainly located between 200 and 300 m. The highest occurrence frequency appears at approximately 250 m, exceeding 14%. This height range is generally near the top of the stable boundary layer, where vertical momentum exchange and wind shear are enhanced. Figure 6c illustrates the directional distribution of LLJs. The observed LLJs are mainly concentrated in the easterly and east-northeasterly directions. The easterly direction dominates, with an occurrence frequency close to 60%. In terms of wind speed intensity, LLJs with speeds of 8–10 m s^{-1} occur most frequently, followed by those with speeds of 6–8 m s^{-1}. These results indicate that LLJs in the study region exhibit a pronounced directional preference and are mainly characterized by moderate-intensity easterly flows.

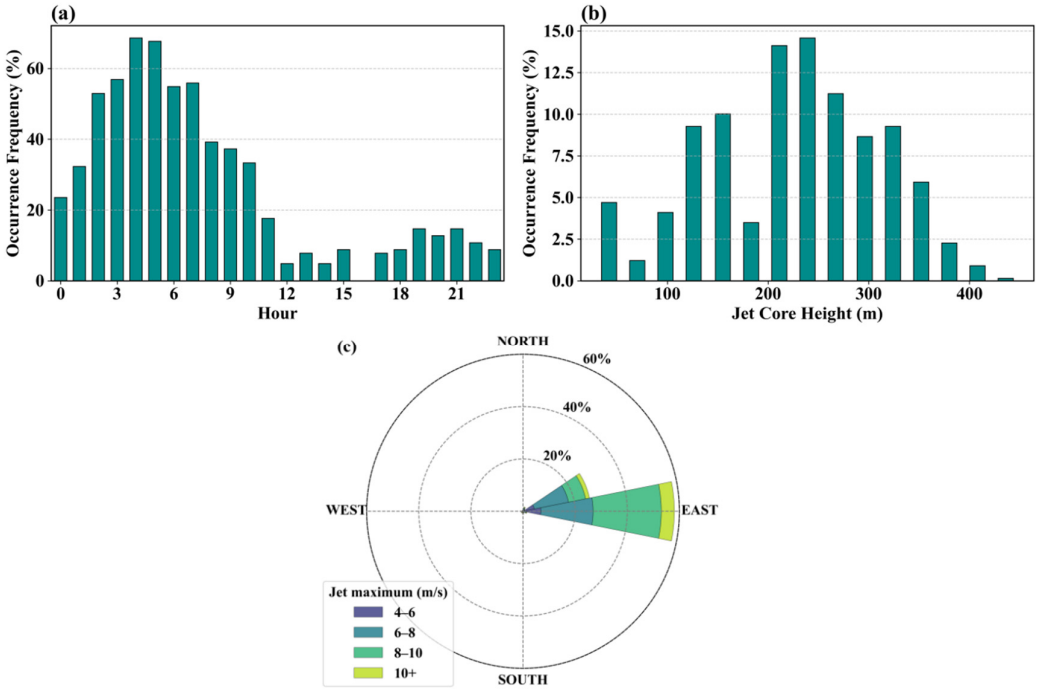


Figure 6. Characteristics of overall LLJs. (**a**) Diurnal variation in LLJ occurrence frequency; (**b**) variation in the occurrence frequency of jet core heights; (**c**) distribution of jet speed maximum and jet direction.

The composite wind profile derived from 16 LLJ events reveals a clear single-peak vertical structure in the study region (Figure 7a). The wind speed increases with height and reaches its maximum at approximately 270 m. Above the jet core, the wind speed gradually decreases with increasing height. In the lower layer (0–100 m), the wind speed remains relatively weak. It increases rapidly above this layer and forms a distinct low-level wind speed maximum. Although individual LLJ events exhibit variations in jet intensity and core height, the composite profile maintains a consistent vertical pattern after averaging. This indicates that the selected LLJ cases share a common statistical

vertical structure. A Gaussian function was applied to parameterize the composite wind profile:

$$U(z)=4.75+2.72\exp\left(-\frac{(z-269.9)^2}{2(177.1)^2}\right) \quad (21)$$

where U_0, U_j, z_j, and σ represent the background wind speed, jet enhancement magnitude, jet core height, and vertical scale of the jet structure, respectively. The fitted parameters are U_0 = 4.75 m s^{-1}, U_j = 2.72 m s^{-1}, z_j = 269.9 m, and σ = 177.1 m. The parameterized profile provides a simple representation of the mean vertical wind structure of LLJs in the study region.

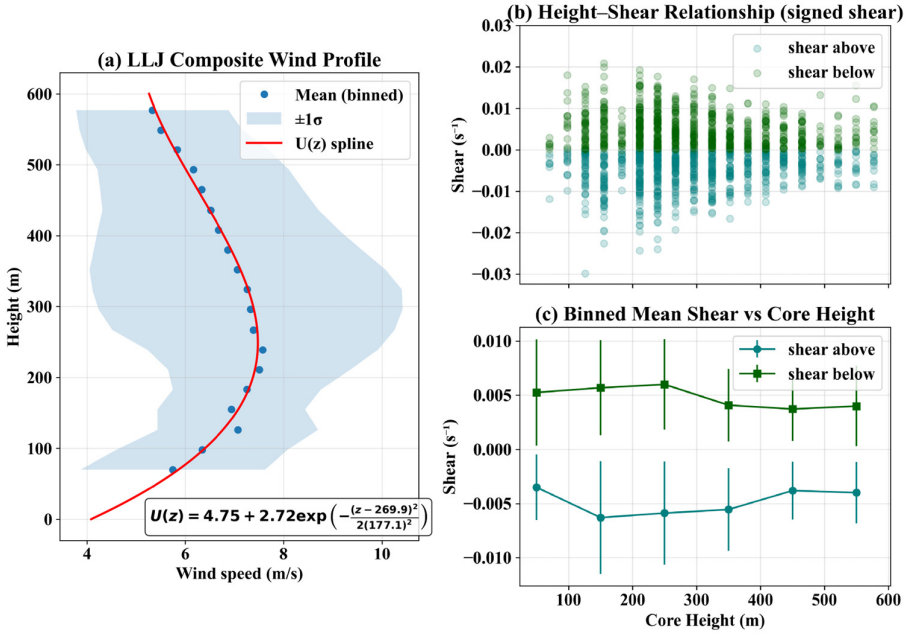


Figure 7. (**a**) Composite wind profile of low-level jets (LLJs). The blue dots represent the binned mean wind speeds, the shaded area denotes the standard deviation (±1σ), and the red curve indicates the fitted wind speed profile. (**b**) The distribution of low-level wind shear above and below the LLJ core at different core heights; (**c**) the binned mean shear variations with LLJ core height.

The relationship between LLJ core height and vertical shear above and below the jet core was further examined (Figure 7b,c). The upper-level and lower-level shear show opposite signs. The shear above the jet core is mainly negative, indicating a decrease in wind speed with height above the core. In contrast, the shear below the jet core is predominantly positive, indicating an increase in wind speed toward the jet core. The mean upper-level shear varies within a relatively narrow range across different core heights. It reaches relatively stronger values around 200–300 m and gradually weakens at higher core heights. The lower-level shear shows a similar dependence, with relatively larger values occurring for LLJs with core heights of approximately 200–300 m. It then slightly decreases as the core height increases.

These results suggest that LLJ core height is associated with the distribution of vertical shear, but the relationship is not simply linear. LLJs with intermediate core heights exhibit stronger wind gradients above and below the jet core. The combined characteristics of the composite wind profile and shear distribution indicate that the jet core height influences not only the location of maximum wind speed but also the vertical distribution of wind gradients around the LLJ core.

The relationships between LLJ shear coefficients and characteristic wind parameters are further examined in Figure 8. A significant negative relationship exists between positive and negative shear coefficients (Figure 8a), indicating a coupled variation between the shear structures below and above the LLJ core. Stronger positive shear below the LLJ core is generally accompanied by stronger negative shear above the core, indicating that the vertical shear distribution is controlled by the overall LLJ wind profile rather than by independent layer processes.

The LLJ core wind speed shows an asymmetric influence on the vertical shear distribution (Figure 8b). Increasing core wind speed is associated with enhanced negative shear above the jet core, whereas positive shear below the core exhibits a weak decreasing tendency. This suggests that stronger LLJs are mainly characterized by intensified wind speed reduction above the jet core.

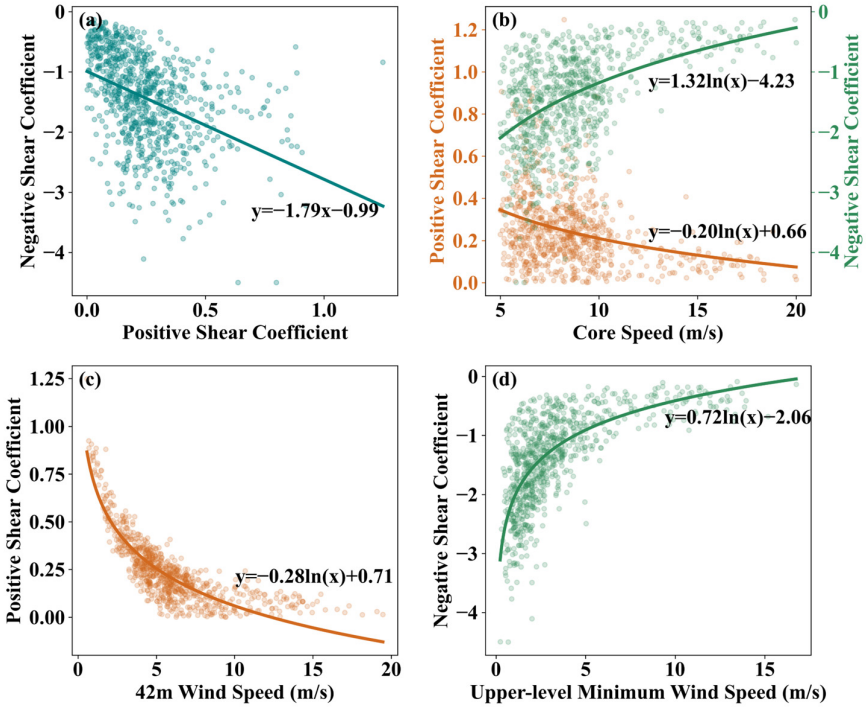


Figure 8. (**a**) Correlation between positive and negative shear coefficients. (**b**) Correlation of positive and negative shear coefficients with LLJ core wind speed. (**c**) Correlation between positive shear coefficient and 42 m surface wind speed. (**d**) Correlation between negative shear coefficient and upper-level minimum wind speed above the LLJ core. The solid curves represent logarithmic fitting results.

The near-surface wind speed also affects the lower-level shear structure (Figure 8c). The positive shear coefficient decreases logarithmically with increasing 42 m wind speed, indicating reduced wind speed contrast between the surface layer and the LLJ core. In contrast, the negative shear coefficient decreases with increasing upper-level minimum wind speed (Figure 8d), suggesting that stronger winds above the LLJ core weaken the upper-level wind gradient.

The temporal relationship between LLJ intensity and LLWS was further examined by aligning individual LLJ events according to their maximum core wind speed (Figure 9). The composite evolution shows that LLWS generally increases during the strengthening stage of LLJ and reaches enhanced values around the LLJ maximum, suggesting a similar temporal evolution between LLJ development and low-level wind shear enhancement.

However, the peak occurrence time of LLWS exhibits considerable variability among individual events. The mean LLWS peak offset relative to the LLJ maximum is −23.5 min, while the median offset is 0 min. This indicates that LLWS and LLJ peaks are generally concurrent, although some cases exhibit earlier or later LLWS maxima. The large spread of peak offsets (standard deviation of 91 min) indicates substantial variability among individual events.

The lag-correlation analysis was further applied to examine the temporal consistency between LLJ intensity and LLWS evolution. The correlation coefficients remained relatively low across different lag times, indicating that LLWS does not exhibit a consistent response time to changes in LLJ intensity. This result suggests that the development of LLWS is associated with LLJ evolution but is also modulated by the detailed vertical wind structure and boundary-layer processes. Therefore, LLJ intensity alone cannot fully determine LLWS evolution, and the vertical distribution of wind speed gradients may play a more important role in controlling LLWS intensity.

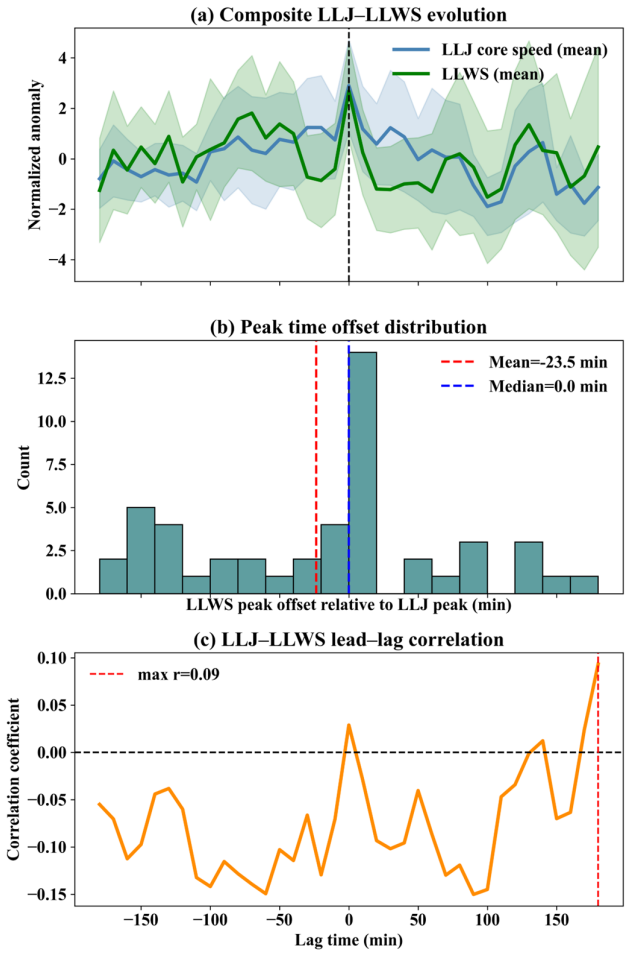


Figure 9. Lead–lag relationship between LLJ core intensity and LLWS evolution. (**a**) The composite temporal evolution of LLJ core speed and LLWS, shaded areas represent the 95% confidence intervals calculated from the 16 independent LLJ events; (**b**) the distribution of peak time differences between LLJ and LLWS; (**c**) the lagged correlation between LLJ intensity and LLWS.

3.3. Typical Case

Figure 10 presents a representative case of low-level wind shear (LLWS) associated with the development of a low-level jet (LLJ) on 13 March 2024. Panels (a)–(c) illustrate

the temporal evolution of the wind field, vertical wind shear, and turbulent kinetic energy (TKE), respectively.

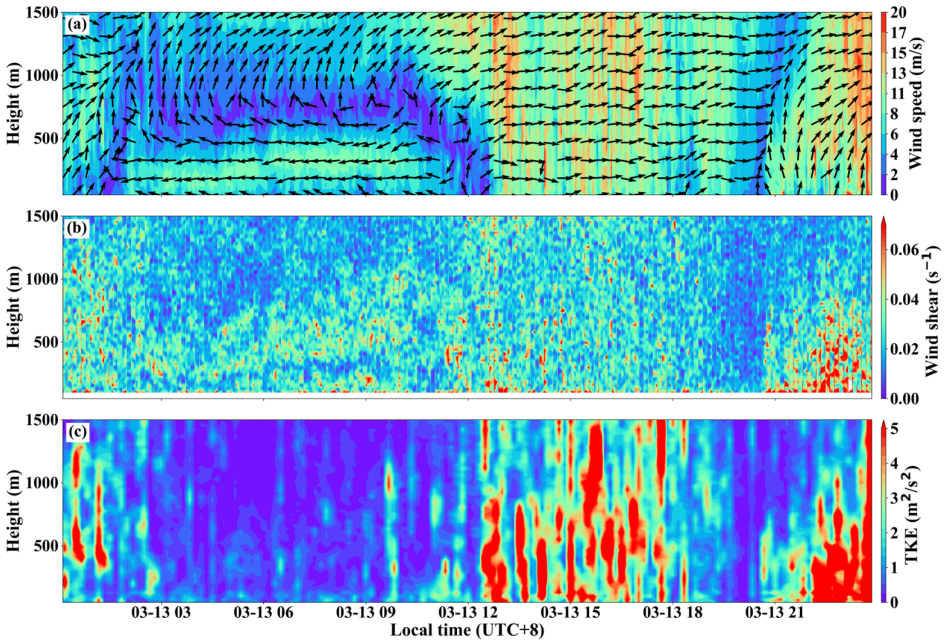


Figure 10. Evolution of low-level wind field characteristics observed by DBS on 13 March 2024. (**a**) Wind profile, with black arrows indicating wind vectors; (**b**) wind shear distribution; (**c**) turbulent kinetic energy distribution.

As illustrated in Figure 10a, the background wind field exhibited distinct diurnal variations before LLJ formation. At 0000 LT, westerly winds prevailed in the upper boundary layer. Meanwhile, southwesterly flow dominated near the surface. This resulted in pronounced vertical directional wind shear. During 0000–0130 LT, the low-level wind direction showed substantial fluctuations. This period represented a transitional stage before LLJ development. At approximately 0300 LT, a well-defined LLJ developed within the nocturnal boundary layer. Easterly flow became dominant in the lower boundary layer. In contrast, westerly winds persisted above the boundary layer. This produced a pronounced vertical decoupling of wind directions. The boundary layer remained relatively shallow during this stage, with a depth of approximately 500 m. The LLJ core was initially embedded within this shallow layer. The maximum wind speeds reached 6–8 m s^{-1}. As the event evolved, the LLJ gradually intensified. The jet core also migrated upward. This evolution represents a typical nocturnal LLJ development process, characterized by progressive strengthening and vertical expansion of the jet structure. After approximately 1000 LT, the LLJ gradually decayed. This weakening was accompanied by a decrease in boundary layer height. By 1200 LT, the wind direction throughout the boundary layer shifted back to westerly. Wind speed increased rapidly during this period. The strongest winds of the day occurred during the afternoon, when maximum wind speeds exceeded 20 m s^{-1}. During the evening (approximately 2000 LT), the low-level flow shifted to southerly. Meanwhile, relatively strong winds (>11 m s^{-1}) persisted throughout the lower troposphere.

The evolution of low-level wind shear during this LLJ event is further illustrated in Figure 10b. During the LLJ formation and mature stages (approximately 0300–1000 LT), enhanced wind shear was mainly confined below 600 m. The wind shear intensity increased rapidly following LLJ development. It reached maximum values exceeding 0.08 s^{-1}. After 1000 LT, the LLJ gradually weakened, and the low-level wind shear decreased

accordingly. The temporal consistency between LLJ intensity and wind shear variation indicates that the enhanced vertical wind speed and directional gradients associated with the LLJ played a key role in generating strong low-level wind shear.

Figure 10c presents the temporal and vertical evolution of turbulent kinetic energy (TKE) during the LLJ event. In contrast to the strong enhancement of wind shear, the increase in TKE within the LLJ layer remained relatively limited during the LLJ formation and mature stages. Although the development of the LLJ generated pronounced vertical wind gradients, the corresponding increase in turbulent activity was weak, particularly below the core region of the jet. The enhanced wind shear did not always correspond to a proportional increase in turbulence intensity, indicating that the development of turbulence was not solely determined by shear intensity. Although LLJ-induced wind shear provides a mechanical source for turbulence generation, the observed TKE distribution suggests that turbulence evolution may also be influenced by other factors, such as atmospheric stability and local terrain effects [42].

Figure 11 presents a typical case of LLJ evolution and its associated low-level wind shear characteristics based on PPI-mode observations. During 02:10–10:50 LT (Figure 11a), the high wind-speed region was mainly distributed in the eastern sector, indicating a dominant easterly LLJ. Wind speeds in the eastern region reached approximately 15 m s^{-1}, whereas the southern sector remained relatively weak, with wind speeds generally ranging from 0 to 5 m s^{-1}. The corresponding wind shear distribution (Figure 11d) showed a similar spatial pattern, with stronger values concentrated in the eastern sector and reaching up to 0.18 s^{-1}, indicating enhanced horizontal wind gradients associated with the easterly LLJ. During 10:50–21:00 LT (Figure 11b), the high wind-speed area shifted from the eastern sector toward the western sector, suggesting a pronounced transition in the spatial distribution of high-speed flows within the valley environment. Meanwhile, the overall wind speed increased, with maximum values exceeding 18 m s^{-1} in the western sector, while the southern region remained characterized by relatively weak winds. During 00:00–02:10 LT and 21:00–23:59 LT (Figure 11c), the wind field further rotated, with the strongest winds shifting toward the southern sector. Wind speeds in this region exceeded 18 m s^{-1}. The associated wind shear (Figure 11f) was also enhanced over the southern sector, with maximum values exceeding 0.18 s^{-1} and a broader spatial extent compared with the previous periods. These results demonstrate the diurnal variation in valley wind circulation and the redistribution of high-speed flow regions and its close correspondence with the spatial distribution of low-level wind shear in the valley environment.

Overall, this case shows a clear diurnal evolution of the valley wind field, with the wind-speed maximum migrating from the eastern sector in the early morning, to the western sector in the afternoon, and finally to the southern sector at night. The easterly LLJ in the early morning is associated with enhanced wind shear, while the subsequent western and southern high-speed flows reflect changes in valley circulation.

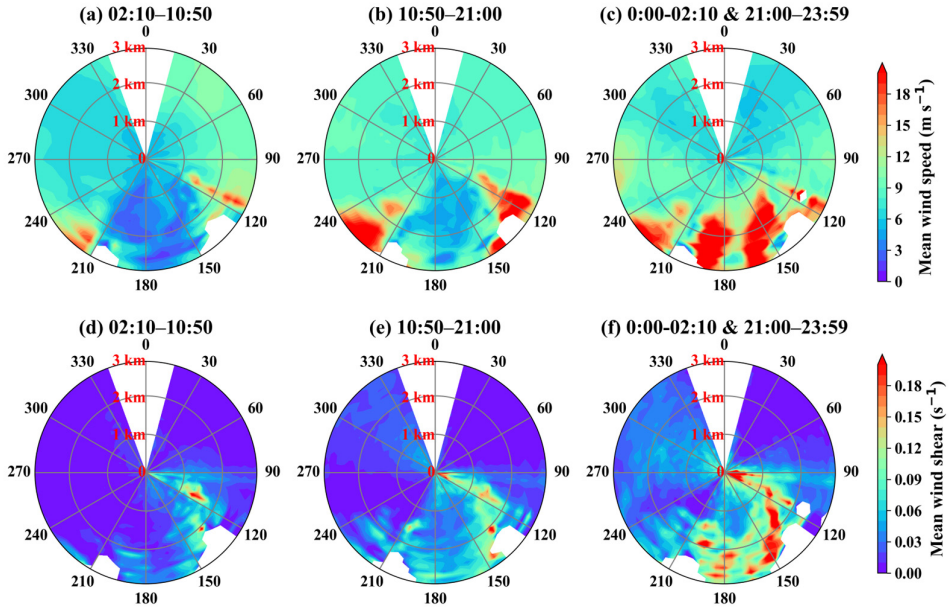


Figure 11. The mean wind speed (**a**–**c**) and mean wind shear (**d**–**f**) distributions during different periods in the PPI mode: (**a**,**d**) 02:10–10:50 LT, (**b**,**e**) 10:50–21:00 LT, and (**c**,**f**) 00:00–02:10 LT and 21:00–23:59 LT. White areas indicate missing data.

4. Conclusions

In this study, high-resolution Doppler lidar observations were used to investigate the characteristics of low-level wind fields, low-level jets (LLJs), and low-level wind shear (LLWS) in the valley environment of Lhasa Gonggar Airport during March–April 2024. The main conclusions are summarized as follows:

The low-level wind field exhibited pronounced diurnal variations in both wind direction and speed. Easterly flows dominated from early morning to late morning, while westerly flows prevailed in the afternoon and southerly flows occurred mainly at night. These directional transitions indicate pronounced diurnal evolution of the local low-level circulation. A total of 16 LLJ events were identified from the high-resolution wind observations. Most LLJ events occurred during 02:00–10:00 LT, with the highest occurrence frequency around 04:00–05:00 LT. The LLJ cores were mainly concentrated at 200–300 m, with a maximum occurrence near 250 m. The observed LLJs were primarily easterly, and moderate-intensity jets with wind speeds of 8–10 m s^{-1} occurred most frequently. LLJ evolution was closely associated with LLWS development. Enhanced LLWS generally occurred during the strengthening and mature stages of LLJs, when intensified wind speed and directional gradients produced stronger vertical wind shear. The vertical distribution of wind shear was influenced by LLJ characteristics, including jet core height, jet intensity, and the surrounding wind structure. Typical cases further demonstrated that the spatial distribution of LLWS followed the evolution of LLJ-induced wind field changes, with the high wind-speed region migrating from the eastern sector in the morning to the western sector in the afternoon and finally to the southern sector at night. Overall, this study highlights the important role of valley-induced LLJ processes in modulating low-level wind shear characteristics and provides observational evidence for understanding and monitoring wind shear hazards at high-altitude airports using Doppler lidar.

Author Contributions: Conceptualization, H.D. and D.Z.; methodology, H.D. and D.Z.; software, H.D.; validation, H.D. and T.W.; formal analysis, H.D.; investigation, H.D., L.D. and X.P.; data curation, H.D. and L.D.; writing—original draft preparation, H.D.; writing—review and editing,

H.D. and D.Z.; visualization, H.D.; supervision, D.Z.; project administration, D.Z. All authors have read and agreed to the published version of the manuscript.

Funding: This research was funded by the China Postdoctoral Science Foundation (grant number 2022TQ0332), the National Natural Science Foundation of China (grant number 42307144), and the Fundamental Research Funds for the Central Universities (grant number 24CAFUC07001).

Data Availability Statement: The datasets generated and analyzed during the current study are not publicly available due to institutional restrictions but are available from the corresponding author upon reasonable request.

Acknowledgments: The authors would like to thank Yongjing Ma, Siyan Jia, and Liming Li for their contributions to the research resource support, observational work, and manuscript review and editing.

Conflicts of Interest: The authors declare no conflicts of interest.

Reference

1. International Civil Aviation Organization (ICAO). *Manual on Low-Level Wind Shear*; ICAO: Montreal, QC, Canada, 2005.
2. Shun, C.M.; Chan, P.W. Applications of an Infrared Doppler Lidar in Detection of Wind Shear. *J. Atmos. Ocean. Technol.* **2008**, *25*, 637–655.
3. Golding, W.L. Low-Level Windshear and Its Impact on Airlines. *J. Aviat./Aerosp. Educ. Res.* **2005**, *14*, 35–45.
4. Nechaj, P.; Gaál, L.; Bartok, J.; Vorobyeva, O.; Gera, M.; Kelemen, M.; Polishchuk, V. Monitoring of Low-Level Wind Shear by Ground-Based 3D Lidar for Increased Flight Safety, Protection of Human Lives and Health. *Int. J. Environ. Res. Public Health* **2019**, *16*, 4584.
5. Iijima, T.; Matayoshi, N.; Ueda, S. Operational Concept and Validation of a New Airport Low-Level Wind Information System. *Aeronaut. J.* **2020**, *124*, 975–1015.
6. McCarthy, J.; Serafin, R.; Wilson, J.; Evans, C.; Kessinger, W.; Mahoney, W.P. Addressing the Microburst Threat to Aviation: Research-to-Operations Success Story. *Bull. Am. Meteorol. Soc.* **2022**, *103*, E2845–E2861.
7. Marke, T.; Crewell, S.; Schemann, V.; Schween, J.H.; Tuononen, M. Long-Term Observations and High-Resolution Modeling of Midlatitude Nocturnal Boundary Layer Processes Connected to Low-Level Jets. *J. Appl. Meteorol. Climatol.* **2018**, *57*, 1155–1170.
8. Chan, P.W.; Hon, K.K.; Li, Q.S. Low-Level Windshear Associated with Atmospheric Boundary Layer Jets—Case Studies. *Atmósfera* **2021**, *34*, 461–490.
9. Chan, P.W.; Hon, K.K.; Li, Q.S. A Comprehensive Study of Terrain-Disrupted Airflow at Hong Kong International Airport—Observations and Numerical Simulations. *Weather* **2020**, *75*, 199–206.
10. Louis, K.S.; Guan, Y.; Li, L.K.B. RANS Simulations of Terrain-Disrupted Turbulent Airflow at Hong Kong International Airport. *Comput. Math. Appl.* **2021**, *81*, 737–758.
11. Shu, Z.R.; Li, Q.S.; He, Y.C.; Chan, P.W. Investigation of Low-Level Jet Characteristics Based on Wind Profiler Observations. *J. Wind Eng. Ind. Aerodyn.* **2018**, *174*, 369–381.
12. Yang, B.; Finn, D.; Rich, J.; Gao, Z.; Liu, H. Effects of Low-Level Jets on Near-Surface Turbulence and Wind Direction Changes in the Nocturnal Boundary Layer. *J. Geophys. Res. Atmos.* **2023**, *128*, e2022JD037657.
13. Carroll, B.J.; Demoz, B.B.; Delgado, R. An Overview of Low-Level Jet Winds and Corresponding Mixed Layer Depths during PECAN. *J. Geophys. Res. Atmos.* **2019**, *124*, 9141–9160.
14. Smith, E.N.; Gebauer, J.G.; Klein, P.M.; Fedorovich, E.; Gibbs, J.A. The Great Plains Low-Level Jet during PECAN: Observed and Simulated Characteristics. *Mon. Weather Rev.* **2019**, *147*, 1845–1869.
15. Chen, Y.; An, J.L.; Lin, J.; Sun, Y.L.; Wang, X.Q.; Wang, Z.F.; Duan, J. Observation of Nocturnal Low-Level Wind Shear and Particulate Matter in Urban Beijing Using a Doppler Wind Lidar. *Atmos. Ocean. Sci. Lett.* **2017**, *10*, 411–417.
16. Pichugina, Y.L.; Banta, R.M.; Brewer, W.A.; Sandberg, S.P.; Hardesty, R.M. Doppler Lidar-Based Wind-Profile Measurement System for Offshore Wind-Energy and Other Marine Boundary Layer Applications. *J. Appl. Meteorol. Climatol.* **2012**, *51*, 327–349.
17. Luiz, E.W.; Fiedler, S. Global Climatology of Low-Level Jets: Occurrence, Characteristics, and Meteorological Drivers. *J. Geophys. Res. Atmos.* **2024**, *129*, e2023JD040262.
18. Banta, R.M.; Newsom, R.K.; Lundquist, J.K.; Pichugina, Y.L.; Coulter, R.L.; Mahrt, L. Nocturnal Low-Level Jet Characteristics over Kansas during CASES-99. *Bound.-Layer Meteorol.* **2002**, *105*, 221–252.

19. Shapiro, A.; Fedorovich, E.; Rahimi, S. A Unified Theory for the Great Plains Nocturnal Low-Level Jet. *J. Atmos. Sci.* **2016**, *73*, 3037–3057.
20. Basic, I.; Jadhav, H.; Singh, J.; Schmidli, J. Impact of Small-Scale Orography on Deep Boundary Layer Evolution and Structure over the Tibetan Plateau. *Atmos. Chem. Phys.* **2026**, *26*, 2007–2025.
21. Zhou, W.; Lou, W.; Huang, M.; Liu, J.; Liang, M. Two-Year Wind Field Measurements near the Ground at a Site of the Tibetan Plateau. *J. Wind Eng. Ind. Aerodyn.* **2024**, *245*, 105602.
22. Mahrt, L. Nocturnal Boundary-Layer Regimes. *Bound.-Layer Meteorol.* **1999**, *88*, 255–278.
23. Fernando, H.J.S.; Weil, J.C. Whither the Stable Boundary Layer?: A Shift in the Research Agenda. *Bull. Am. Meteorol. Soc.* **2010**, *91*, 1475–1484.
24. Wang, C.X.; Ma, Y.M.; Han, C.B. Research on the Structure and Development Mechanism of the Atmospheric Boundary Layer over the Tibetan Plateau. *Adv. Earth Sci.* **2023**, *38*, 414.
25. Che, J.; Zhao, P. Characteristics of the Summer Atmospheric Boundary Layer Height over the Tibetan Plateau and Influential Factors. *Atmos. Chem. Phys.* **2021**, *21*, 5253–5268.
26. Chen, X.; Añel, J.A.; Su, Z.; de la Torre, L.; Kelder, H.; van Peet, J.; Ma, Y. The Deep Atmospheric Boundary Layer and Its Significance to the Stratosphere and Troposphere Exchange over the Tibetan Plateau. *PLoS ONE* **2013**, *8*, e56909.
27. Ding, J.; Cuo, L.; Zhang, Y.; Zhang, C. Varied Spatiotemporal Changes in Wind Speed over the Tibetan Plateau and Its Surroundings in the Past Decades. *Int. J. Climatol.* **2021**, *41*, 5956–5976.
28. Guo, X.; Wang, L.; Li, D.; Li, X. Elevation-Dependent Reductions in Wind Speed over and around the Tibetan Plateau. *Int. J. Climatol.* **2017**, *37*, 2370–2383.
29. Zheng, J.; Liu, Y.; Peng, T.; Wan, X.; Huang, X.; Wang, Y.; Che, Y.; Xu, D. Investigating Wind Characteristics and Temporal Variations in the Lower Troposphere over the Northeastern Qinghai–Tibet Plateau Using a Doppler LiDAR. *Remote Sens.* **2024**, *16*, 1840.
30. Huang, X.; Zheng, J.; Shao, A.; Xu, D.; Tian, W.; Li, J. Study of Low-Level Wind Shear at a Qinghai-Tibetan Plateau Airport. *Atmos. Res.* **2024**, *311*, 107680.
31. Wu, B.; Li, Z.; Ju, T.; Zhang, H. Characteristics of Low-Level Jets during 2015–2016 and the Effect on Fog in Tianjin. *Atmos. Res.* **2020**, *245*, 105102.
32. Bryukhanov, I.; Loktyushin, O.; Ni, E.; Samokhvalov, I.; Pustovalov, K.; Kuchinskaia, O. Comparison of the Contrail Drift Parameters Calculated Based on the Radiosonde Observation and ERA5 Reanalysis Data. *Atmosphere* **2024**, *15*, 1487.
33. Ding, H.; Zhao, D.; Duan, L.; Wu, J.; Sang, W.; Liu, G.; Wang, T.; Zhang, S.; Li, Y. Low-Level Wind Shear Characteristics in the Qinghai-Tibet Plateau by Long-Term Wind Lidar Observations and the Improved Algorithm. *Atmosphere* **2026**, *17*, 6.
34. Liu, Z.; Barlow, J.F.; Chan, P.W.; Fung, J.C.H.; Li, Y.; Ren, C.; Mak, H.W.L.; Ng, E. A Review of Progress and Applications of Pulsed Doppler Wind LiDARs. *Remote Sens.* **2019**, *11*, 2522.
35. Graßl, S.; Ritter, C.; Schulz, A. The Nature of the Ny-Alesund Wind Field Analysed by High-Resolution Windlidar Data. *Remote Sens.* **2022**, *14*, 3771.
36. Browning, K.A.; Wexler, R. The Determination of Kinematic Properties of a Wind Field Using Doppler Radar. *J. Appl. Meteorol.* **1968**, *7*, 105–113.
37. Gutierrez, W.; Ruiz-Columbie, A.; Tutkun, M.; Castillo, L. Impacts of the low-level jet's negative wind shear on the wind turbine. *Wind Energy Sci.* **2017**, *2*, 533–545.
38. Rehman, S.; Al-Abbadi, N.M. Wind shear coefficients and their effect on energy production. *Energy Convers. Manag.* **2005**, *46*, 2578–2591.
39. Bonner, W.D. Climatology of the Low Level Jet. *Mon. Weather Rev.* **1968**, *96*, 833–850.
40. Dickison, R.B.B.; Neumann, H.H. The Occurrence of Nocturnal Low-Level Jets in New England and the Canadian Maritimes. *Atmos.-Ocean* **1982**, *20*, 287–300.
41. Xue, Y.; He, J.; Chan, P.; Li, Q. Multi-Source Observational Study of Wind Shear and Veer at Hong Kong International Airport. *Urban Clim.* **2026**, *65*, 102758.
42. Xian, J.; Qiu, Z.; Luo, H.; Hu, Y.; Lin, X.; Lu, C.; Yang, Y.; Yang, H.; Zhang, N. Turbulent energy budget analysis based on coherent wind lidar observations. *Atmos. Chem. Phys.* **2025**, *25*, 441–457.

Disclaimer/Publisher's Note: The statements, opinions and data contained in all publications are solely those of the individual author(s) and contributor(s) and not of MDPI and/or the editor(s). MDPI and/or the editor(s) disclaim responsibility for any injury to people or property resulting from any ideas, methods, instructions or products referred to in the content.